

RocMLMs: Predicting Rock Properties through Machine Learning Models

Buchanan Kerswell ¹Nestor Cerpa ¹Andréa Tommasi ¹Marguerite Godard
¹José Alberto Padrón-Navarta ²

¹Geosciences Montpellier, University of Montpellier, CNRS, University of Antilles, Place Eugène
Bataillon, 34095 Montpellier, France

²Instituto Andaluz de Ciencias de la Tierra (IACT), CSIC, Avda. de las Palmeras, 4, 18100 Armilla
(Granada), Spain

Key Points:

- RocMLMs predict rock properties up to 10^1 – 10^3 faster than commonly used methods
- RocMLMs trained with Neural Networks are more efficient compared to other regression algorithms
- RocMLM training data show good agreement with PREM and STW105 for an average mantle geotherm

Corresponding author: Buchanan Kerswell, buchanan.kerswell@umontpellier.fr

Abstract

16 Mineral phase transformations significantly alter the bulk density and elastic properties
17 of mantle rocks and consequently have profound effects on mantle dynamics and seis-
18 mic wave propagation. These changes in the physical properties of mantle rocks result
19 from evolution in the equilibrium mineralogical composition, which can be predicted by
20 the minimization of the Gibbs Free Energy with respect to pressure (P), temperature
21 (T), and chemical composition (X). Thus, numerical models that simulate mantle con-
22 vection and/or probe the elastic structure of the Earth’s mantle must account for vary-
23 ing mineralogical compositions to be self-consistent. Yet coupling Gibbs Free Energy min-
24 imization (GFEM) approaches with numerical geodynamic models is currently intractable
25 for high-resolution simulations because execution speeds of widely-used GFEM programs
26 (10^0 – 10^2 ms) are impractical in many cases. As an alternative, this study introduces ma-
27 chine learning models (RocMLMs) that have been trained to predict thermodynamically
28 self-consistent rock properties at arbitrary PTX conditions between 1–28 GPa, 773–2273
29 K, and mantle compositions ranging from fertile (lherzolitic) to refractory (harzburgitic)
30 end-members defined with a large dataset of published mantle compositions. RocMLMs
31 are 10^1 – 10^3 times faster than GFEM calculations or GFEM-based look-up table approaches
32 with equivalent accuracy. Depth profiles of RocMLMs predictions are nearly indistin-
33 guishable from reference models PREM and STW105, demonstrating good agreement
34 between thermodynamic-based predictions of density, V_p , and V_s and geophysical ob-
35 servations. RocMLMs are therefore capable, for the first time, of emulating dynamic evo-
36 lution of density, V_p , and V_s in high-resolution numerical geodynamic models.
37

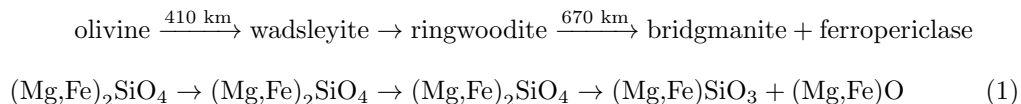
Plain language summary

38 The mineralogical makeup of rocks within Earth’s mantle largely determines how the
39 mantle flows over geologic time, and how it responds to seismic waves triggered by earth-
40 quakes, because mineral assemblages control important rock properties such as density
41 and stiffness (elasticity). The mineralogy of mantle rocks is not constant, however. It
42 changes depending on three factors: pressure, temperature, and the chemical composi-
43 tion of the rock. Thus, it is important for computer simulations of mantle convection to
44 account for the evolution of rock mineralogy. Computer programs that can predict rock
45 properties based on thermodynamic calculations are available, but are generally too slow
46 to be used in high-resolution simulations. As an alternative approach, this study intro-
47

48 duces machine learning models (RocMLMs) that have “learned” how to predict rock prop-
 49 erties (density and elasticity) by “training” on a large dataset of thermodynamic calcu-
 50 lations. We demonstrate that RocMLMs can then predict rock properties up to 10^1 – 10^3
 51 times faster than state-of-the-art methods. We tested RocMLM predictions against ref-
 52 erence mantle models based on observations of seismic waves and found good agreement.
 53 RocMLMs are therefore capable of fast and highly-accurate predictions of changes in rock
 54 properties and can be implemented in high-resolution computer simulations of mantle
 55 convection.

56 1 Introduction

57 The dominant mineral phases in Earth’s mantle are olivine, pyroxene, garnet, wad-
 58 sleyite, ringwoodite, bridgmanite, ferropericlase, calcium silicate perovskite, and MgSiO_3
 59 post-perovskite (e.g., Stixrude and Lithgow-Bertelloni, 2012). Mantle mineralogy evolves
 60 with depth by a series of relatively discontinuous phase transformations that define sharp
 61 transitions in the physical properties of mantle rocks (Ringwood, 1991). The most im-
 62 portant phase transformations occur at depths between 410 km and 670 km beneath Earth’s
 63 surface, defining the transition from the upper to the lower mantle (Equation (1)). This
 64 mantle transition zone (MTZ) is characterized by sharp variations in density and elas-
 65 tic properties that strongly impact mantle convection (Christensen, 1995; Fukao et al.,
 66 2001; Jenkins et al., 2016; Karato et al., 2001; Kuritani et al., 2019; Nakagawa and Buf-
 67 fett, 2005; Ringwood, 1991; Schubert et al., 1975; Tackley et al., 1994; Wang et al., 2015),
 68 and the propagation of teleseismic waves (Dziewoński and Anderson, 1981; Ita and Stixrude,
 69 1992; Ringwood, 1991). The MTZ is therefore an essential feature for modeling mantle
 70 structure and dynamics. With respect to a simple FeO-MgO-SiO_2 chemical system, the
 71 most important MTZ reactions can be written as:



72 These phase changes (e.g., Equation (1)) are often parameterized in numerical geo-
 73 dynamic simulations with simple pressure-temperature (PT)-dependent reaction bound-
 74 aries based on high-pressure experiments (e.g., Agrusta et al., 2017; Ballmer et al., 2015;

75 Christensen, 1995; Čížková and Bina, 2013; Kerswell et al., 2021; Liu et al., 1991; Nak-
76 agawa and Buffett, 2005; Tackley et al., 1994; Torii and Yoshioka, 2007). Alternatively,
77 some numerical geodynamic experiments (e.g., Li et al., 2019; Yang and Faccenda, 2020)
78 use Gibbs Free Energy minimization (GFEM) programs (e.g., Connolly, 2009; Riel et al.,
79 2022) to precompute Lookup Tables of rock properties, which are subsequently referenced
80 to adjust material properties as the numerical experiments evolve. These implementa-
81 tions usually consider fixed ideal mantle compositions, such as pyrolite, and/or approx-
82 imate phase transitions with simple functions. These approaches neglect the PT depen-
83 dency of mineral transitions on natural variations of mantle composition (X) such as vari-
84 ations of Fe-Mg and Al-Ca that may be either primordial or result from melt extraction
85 or reactions during melt transport. Despite these simplifications, these models have cor-
86 roborated that the MTZ is a critical feature impacting subduction dynamics, mantle plume
87 dynamics, and water cycling in the deep Earth.

88 More self-consistent numerical models of mantle convection would track changes
89 in physical properties of mantle rocks by computing GFEM as a function of the evolu-
90 tion of PTX conditions. However, this is currently intractable for high-resolution geo-
91 dynamic models because GFEM programs remain too slow (≥ 4 -228 ms per PTX point)
92 to be applied recursively during a geodynamic simulation (see Supporting Information).
93 Parallelization of GFEM programs can increase efficiency by scaling the number of par-
94 allel processes (Riel et al., 2022), but continuously computing phase relations during geo-
95 dynamic simulations would require GFEM efficiency on the order of $\leq 10^0$ - 10^{-1} ms to
96 be feasible (see Supporting Information), which may be difficult to achieve solely by par-
97 allelisation and/or direct improvements to the current GFEM paradigm.

98 Here, we propose an alternative approach to predicting rock properties based on
99 the use of machine learning models (referred to as RocMLMs) that have been “trained”
100 on a multidimensional dataset of precomputed rock properties using classical (k-Neighbors,
101 Decision Trees) and deep (Neural Network) regression algorithms. These later regres-
102 sion algorithms compress large amounts of thermodynamic information into highly ef-
103 ficient nonlinear functions, allowing RocMLMs to infer (predict) rock properties across
104 arbitrary PTX conditions faster than any current GFEM algorithm. We demonstrate
105 that RocMLMs are thus highly efficient emulators of GFEM programs and are well-suited
106 for predicting bulk rock properties in numerical geodynamic models.

107 This article begins by detailing our method for building, training, and evaluating
 108 RocMLMs. We then demonstrate that RocMLMs can predict densities and seismic ve-
 109 locities in a dry upper mantle and transition zone up to 10^1 – 10^3 times faster than com-
 110 monly used GFEM programs with equivalent accuracies. Finally, we compare RocMLM
 111 predictions with reference models derived from seismological datasets (Dziewoński and
 112 Anderson, 1981; Kustowski et al., 2008) and discuss the accuracy and performance of
 113 RocMLMs with respect to their future implementation in numerical geodynamic mod-
 114 els.

115 2 Methods

116 The following sections describe the methodologies employed in constructing, train-
 117 ing, and assessing RocMLMs, with a focus on four primary objectives. First, define the
 118 size and scope of RocMLM training data to ensure widespread applicability of RocMLMs
 119 to the upper mantle and transition zone (Section 2.1). Second, define a generalized ap-
 120 proach for generating RocMLM training data to ensure applicability to any GFEM pro-
 121 gram (e.g., MAgEMin, Perple_X, and others, Section 2.2). Third, train RocMLMs on
 122 a set of input features that can be routinely computed during geodynamic simulations
 123 to ensure widespread applicability of RocMLMs to various geodynamic codes (Section
 124 2.3). Fourth, rank the overall performance of RocMLMs in terms of accuracy and effi-
 125 ciency (Section 2.4).

126 2.1 RocMLM Training Dataset Design

127 2.1.1 Pressure-Temperature Conditions

128 High-pressure experiments constrain the reaction olivine \rightarrow wadsleyite between 14.0
 129 ± 1.0 GPa and 1600 ± 400 K with Clapeyron slopes between $2.4 \times 10^{-3} \pm 1.4 \times 10^{-3}$ GPa/K
 130 (Akaogi et al., 1989; Katsura and Ito, 1989; Li et al., 2019; Morishima et al., 1994). Like-
 131 wise, the reaction ringwoodite \rightarrow bridgmanite + ferropericlase is constrained between
 132 24.0 ± 1.5 GPa and 1600 ± 400 K with negative Clapeyron slopes between -2.0×10^{-3}
 133 $\pm 1.6 \times 10^{-3}$ GPa/K (Akaogi et al., 2007; Bina and Helffrich, 1994; Hirose, 2002; Ishii et al.,
 134 2018; Ito, 1982; Ito et al., 1990; Ito and Katsura, 1989; Ito and Takahashi, 1989; Kat-
 135 sura et al., 2003; Litasov et al., 2005). We therefore compute RocMLM training data within
 136 a rectangular PT region bounded between 1–28 GPa and 773–2273 K to encompass ex-

137 pected conditions for the entire upper mantle and MTZ—from approximately 30 km to
 138 865 km depth (Figure 1).

139 Figure 1 shows that our training dataset PT range includes PT conditions that are
 140 not expected to exist in neither the Earth’s mantle, nor geodynamic simulations (e.g.,
 141 very cold conditions with thermal gradients ≤ 5 K/km, Cerpa et al., 2022; Maruyama
 142 et al., 1996; Syracuse et al., 2010). Such a large rectangular PT range might be consid-
 143 ered impractical with respect to training efficiency (unnecessary amounts of training data)
 144 and accuracy (outside the bounds of calibrated thermodynamic data) compared to an
 145 irregular PT range bounded between arbitrary geotherms. However, initial sensitivity
 146 tests showed comparable RocMLM performance irrespective of the range of PT condi-
 147 tions used to generate RocMLM training data. Thus, we adopted a regular rectangu-
 148 lar training dataset design because it is computationally convenient and does not dete-
 149 riorate RocMLM accuracy.

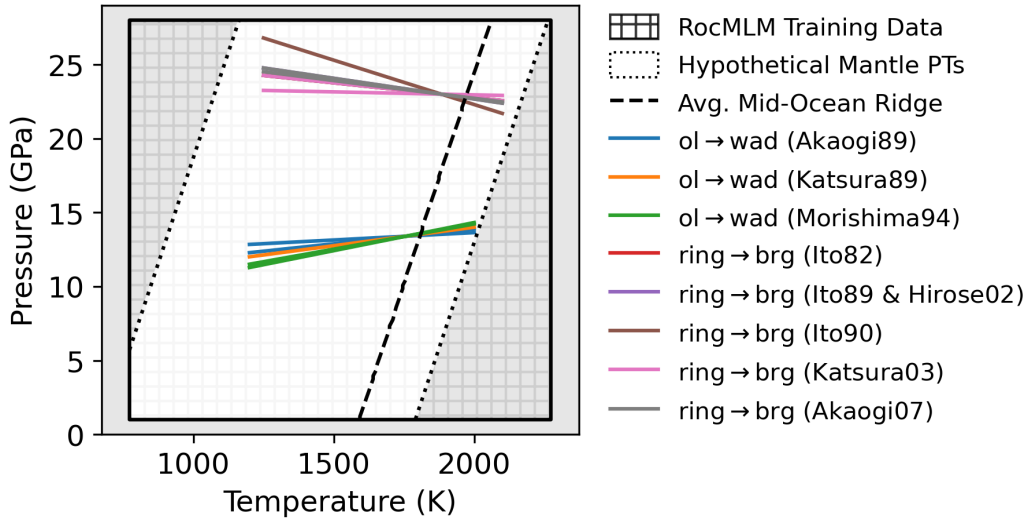


Figure 1: PT diagram showing the range of conditions considered for generating RocMLM training data (hatched region) compared to a range of possible upper mantle conditions (inner white region). The dotted black lines are geotherms with arbitrary mantle potential temperatures of 673 K and 1773 K and a constant adiabatic gradient of 0.5 K/km, representing hypothetical lower and upper bounds for mantle PT conditions (including hypothetical cold lithospheric slabs). The dashed black line is an average geotherm for a mid-ocean ridge (1573 K adiabat). Phase boundaries for the 410 km and 670 km discontinuities (colored lines) are from a compilation by Li et al. (2019).

150 **2.1.2 Bulk Mantle Compositions**

151 We derived an array of synthetic bulk mantle compositions with the aim of encom-
 152 passing the widest range of chemical variability in Earth’s mantle. For this, we applied
 153 a statistical analysis to publicly-available geochemical data from thousands of natural
 154 peridotite samples. The procedure was as follows.

155 Bulk chemical analyses of peridotite samples were downloaded using the Earthchem.org
 156 Search Portal with a single search criterion: “*set sample type > igneous rocks > names*
 157 *from Earthchem categories > igneous-plutonic-ultramafic*”. The search queried 19791 sam-
 158 ples with rock type classifications that we did not modify from their original labels. Sam-
 159 ples lacking analyses for SiO₂, MgO, Al₂O₃, or CaO were excluded from the dataset. All
 160 samples classified as “unknown”, chromitite, limburgite, wehrlite, undifferentiated peri-
 161 dotite, dunite, or pyroxenite were also excluded from the dataset to focus on samples that
 162 are most likely mantellic, that is, residues of partial melting modified (or not) by refer-
 163 tilization, rather than products of fractional crystallization (Bowen, 1915). The data were
 164 grouped according to the remaining rock types (lherzolite and harzburgite) and outliers
 165 were removed from each group using a 1.5 interquartile range threshold applied to each
 166 chemical component. Cr and Ni measured as minor elements (ppm) were converted to
 167 Cr₂O₃ and NiO (wt.%) and all Fe oxides were converted to Fe₂O₃T. Total oxides were
 168 then checked against H₂O, CO₂, and LOI to determine if chemical analyses were per-
 169 formed before or after ignition. Analyses with total oxides summing to $\leq 97\%$ or $\geq 103\%$
 170 were considered erroneous, or otherwise low-quality, and excluded from the dataset. All
 171 analyses were then normalized to a volatile-free basis before converting Fe₂O₃T to FeOT.
 172 After normalization, the final compositional space investigated includes the components
 173 Na₂O-CaO-FeO-MgO-Al₂O₃-SiO₂-TiO₂ (NCFMAST system). The final dataset contains
 174 3111 chemical analyses of classified peridotite samples (Table 1).

175 We applied Principal Component Analysis (PCA) to the standardized peridotite
 176 dataset to reduce its dimensionality from the original 7-oxides space. PCA requires com-
 177 plete data, so samples were first arranged by decreasing MgO and increasing SiO₂ con-
 178 tent and a k-Neighbors algorithm was applied to impute missing oxide analyses, which
 179 were mainly the Na₂O component (see Table 1 for missing analyses counts). Following
 180 common practice, a “z-score normalization” was applied to all oxide components before
 181 running PCA. The first two principal components (PC1 and PC2) explain 78% of the

182 variance of the dataset, which we considered to be sufficient for modeling a broad range
 183 of peridotitic mantle compositions. PC1 separates samples by their TiO₂, Al₂O₃, MgO,
 184 CaO, and Na₂O contents, while PC2 separates samples by SiO₂ and FeO (Figure 2).

185 In this PC space, we drew a mixing line connecting the lherzolite and harzburgite
 186 group centroids (i.e., the median values for PC1 and PC2 for each group). The lherzolite-
 187 harzburgite mixing line was then extended until reaching the approximate location of
 188 the most fertile (Al₂O₃-CaO-TiO₂-rich) and most refractory (MgO-rich, SiO₂-poor) peri-
 189 dotite samples, hereafter referred to as Primitive Synthetic Upper Mantle (PSUM) and
 190 Depleted Synthetic Upper Mantle (DSUM, Figure 2b), respectively. The mixing line ap-
 191 proximates the widest array of mantle compositions derived from the natural rock record
 192 and may be interpreted as representing the first order composition variation in response
 193 to melt extraction (depletion) or addition (refertilization) in the mantle. The mixing line
 194 therefore provides a basis for sampling synthetic bulk mantle compositions directly from
 195 PC space, which were then used to generate RocMLM training data.

Table 1: Summary of the filtered and standardized peridotite dataset from Earth-
 chem.org. Columns with an asterisk are in wt.%. Std = standard deviation, IQR = in-
 terquartile range.

Oxide	Measured	Missing	Min*	Max*	Mean*	Median*	Std*	IQR*
SiO ₂	3111	0	36.7	52	44.1	44.1	1.16	1.24
TiO ₂	2835	276	0	0.268	0.051	0.03	0.05	0.068
Al ₂ O ₃	3111	0	0.023	4.95	1.65	1.31	1.14	1.82
FeO	3111	0	5.98	15.3	8.05	8.01	0.675	0.569
MgO	3111	0	31.8	50.8	43	43.6	2.96	4.38
CaO	3111	0	0.01	5.2	1.46	1.17	1.04	1.66
Na ₂ O	2008	1103	0	0.525	0.127	0.098	0.11	0.171

196 *2.1.3 Reducing Bulk Mantle Compositions to a Single Fertility Index* 197 *Value*

198 Training RocMLMs with either 7 oxide components or two PCs as inputs is pos-
 199 sible. However, our targeted application (e.g., implementing RocMLMs in geodynamic
 200 codes) discourages the use of the two options because in either case it would require track-

201 ing the oxides in numerical geodynamic codes, which is currently impractical. Thus, we
 202 aimed to reduce the dimensionality of the training dataset from nine dimensions (7 ox-
 203 ide components + PT) to three dimensions (1 compositional dimension + PT) by es-
 204 timating the amount of melt extraction (depletion) that might have produced the syn-
 205 thetic bulk mantle compositions in the training dataset. Assuming that all synthetic sam-
 206 ples were derived from a PSUM source, we adopt a simple modal fractional melting model
 207 (after Shaw, 1970):

$$\frac{C_{\text{TiO}_2}^s}{C_{\text{TiO}_2}^0} = R = (1 - F)^{\frac{1}{D_0} - 1} \quad (2)$$

208 where R is the ratio of the TiO_2 concentration of the sample to the initial PSUM source
 209 (Table 2), F is the melt fraction, and $D_0 = 0.05$ is the bulk distribution coefficient for
 210 TiO_2 in peridotite (after Brown and Lesher, 2016). Note that unlike the dataset of nat-
 211 ural peridotite samples, synthetic samples were drawn directly from PC space and their
 212 TiO_2 concentrations (and other oxide components) change monotonically with PC1 from
 213 the initial PSUM source (Figure 2b,c). Synthetic samples therefore represent a smooth
 214 and idealized variability from fertile (PSUM) to depleted (DSUM) mantle compositions
 215 that captures the average variation in natural peridotite samples.

216 A Fertility Index (ξ) is calculated by rearranging Equation (2) for F and subtract-
 217 ing F from 1:

$$\xi = 1 - F = R^{\frac{1}{\frac{1}{D_0} - 1}} \quad (3)$$

218 Training RocMLMs on ξ instead of seven oxide components is beneficial for two
 219 reasons: 1) it greatly increases RocMLM efficiency and 2) unlike oxide components or
 220 PCs, melt fraction is routinely implemented in numerical geodynamic simulations (e.g.,
 221 Cerpa et al., 2019; Gerya and Yuen, 2003; Kelley et al., 2010; Li et al., 2019; Sizova et al.,
 222 2010; Yang and Faccenda, 2020). Likewise, tracking the depletion/fertility of the man-
 223 tle in geodynamics models with Lagrangian tracers and/or compositional fields is more
 224 conceivable (Agrusta et al., 2015; Cagnioncle et al., 2007; Gerya and Meilick, 2011; Tack-
 225 ley and Xie, 2003). Although we chose ξ for RocMLM training, ξ and F represent op-
 226 posite reference frames for the same time-integrated melting process, and are therefore

227
228

interchangeable. This approach offers a generalized solution for coupling RocMLMs to geodynamic codes.

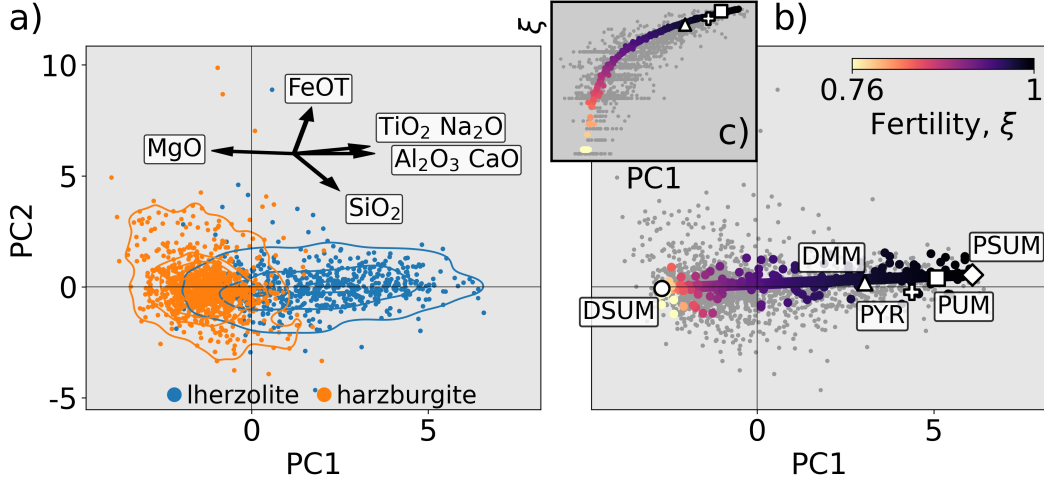


Figure 2: PC1-PC2 diagrams showing the standardized geochemical dataset of natural peridotite samples (a) and a mixing array between hypothetical end-member mantle compositions Primitive Synthetic Upper Mantle (PSUM) and Depleted Synthetic Upper Mantle (DSUM, b). Black arrows in (a) indicate PCA loading vectors. Colored data points in (b) are the synthetic mantle compositions used to train RocMLMs, which were sampled independently from the natural peridotite samples (gray data points). The inset (c) shows how the Fertility Index (ξ) changes nonlinearly with PC1. DMM, PUM, and PYR are from Table 2.

229
230
231
232
233
234
235
236
237
238
239
240
241
242

The melting model in Equation (2) is oversimplified since it assumes: 1) melt is instantaneously removed from the source region, 2) D_0 is constant, and 3) minerals melt in the same proportions that they exist in the source rock. It nevertheless provides an efficient parameterization of the variation in mantle composition as a function of melt extraction and addition. Equation (2) predicts that a Depleted MORB Mantle (DMM) composition is produced through a time-integrated 2.2% melt extraction from a Primitive Upper Mantle (PUM) source (Table 2). This result is consistent with the degree of depletion inferred from trace element patterns and mass balance constraints (2-3% melt removal from PUM, Workman and Hart, 2005). We therefore consider ξ an adequate first-order proxy for describing the variations in bulk mantle composition used in our RocMLM training dataset. However, given that TiO_2 concentrations are strongly affected by reactive melt transport (e.g., Le Roux et al., 2007), ξ may only be estimated for the average compositional trend as expressed in PC1-PC2 space, rather than on individual peridotite samples.

Table 2: Hypothetical upper mantle end-member compositions. Columns with an asterisk are in wt.%. Depleted MORB Mantle (DMM) is from Workman and Hart (2005), Primitive Upper Mantle (PUM) is from Sun and McDonough (1989), and Pyrolite (PYR) is from Green (1979). Primitive Synthetic Upper Mantle (PSUM) and Depleted Synthetic Upper Mantle (DSUM), are end-member compositions derived in this study.

Sample	SiO ₂ *	TiO ₂ *	Al ₂ O ₃ *	FeOT*	MgO*	CaO*	Na ₂ O*	ξ
DSUM	44.1	0.0012	0.261	7.96	47.4	0.22	0.042	0.764
DMM	44.7	0.13	3.98	8.18	38.7	3.17	0.13	0.974
PYR	45	0.16	4.4	7.6	38.8	3.4	0.34	0.984
PUM	44.9	0.2	4.44	8.03	37.7	3.54	0.36	0.996
PSUM	46.2	0.216	4.88	8.88	35.2	4.34	0.33	1

2.2 Generating RocMLM Training Data

We used the GFEM program *Perple_X* (version 7.0.9, Connolly, 2009) to generate RocMLM training data across PT conditions as described in Section 2.1.1 and synthetic bulk mantle compositions as described in Section 2.1.2. The *Perple_X* calculations were constrained to the Na₂O-CaO-FeO-MgO-Al₂O₃-SiO₂ (NCFMAS) chemical system to comply with the thermodynamic data and solution models of Stixrude and Lithgow-Bertelloni (2022). The Stixrude and Lithgow-Bertelloni (2022) dataset (*stx21ver.dat*) was used because our initial tests with alternative thermodynamic datasets (*hp02ver.dat* and *hp633ver.dat*, Connolly and Kerrick, 2002; Holland et al., 2018; Holland and Powell, 2001) failed to reproduce the seismic wave velocities of geophysical reference models (PREM and STW105, Dziewoński and Anderson, 1981; Kustowski et al., 2008) with sufficient accuracy because these datasets lack a parametrization of the shear moduli of the minerals phases. Note that our *Perple_X* calculations ignored TiO₂, which was initially included to define ξ and derive synthetic bulk mantle compositions. Despite being measured as a major oxide component, the average TiO₂ content of our standardized samples is 0.05 ± 0.1 wt.% (2σ , Table 1). Such small concentrations of TiO₂ may safely be ignored in phase relation calculations with negligible effects on the RocMLM training dataset.

The *Perple_X* models used to generate the present RocMLM training database included equations of state for solution phases: olivine, plagioclase, spinel, clinopyroxene,

262 wadsleyite, ringwoodite, perovskite, ferropericlase, high-pressure C2/c pyroxene, orthopy-
 263 roxene, akimotoite, post-perovskite, Ca-ferrite, garnet, and Na-Al phase. Melt was not
 264 considered due to the absence of melt models in the Stixrude and Lithgow-Bertelloni (2022)
 265 dataset, but may be considered in future versions of training datasets if the elastic pa-
 266 rameters in hp02ver.dat are corrected. Once configured, Perple_X generated RocMLM
 267 training data (density, as well as P- and S-wave seismic velocities) by minimizing the to-
 268 tal Gibbs Free Energy of a multicomponent multiphase thermodynamic system at fixed
 269 PTX conditions (Gibbs, 1878; Spear, 1993). The reader is referred to Connolly (2009)
 270 and Riel et al. (2022) for a complete description of the GFEM problem.

271 In principle, applying identical sets of solution phase models, thermodynamic data,
 272 and bulk compositions will define identical Gibbs Free Energy hyperplanes. This implies
 273 that any GFEM algorithm should converge on identical phase relations. Thus, although
 274 this study uses Perple_X exclusively, an identical set of training data can be generated
 275 by applying the procedures outlined above to other GFEM programs. Note that RocMLM
 276 capabilities and performance are primarily dependent on the size and the range of PTX
 277 conditions of the training dataset, not on the choice of GFEM algorithm.

278 **2.3 Training RocMLMs**

279 RocMLM training data were preprocessed using the following procedure. First, two-
 280 dimensional grids of rock properties (“pseudosections”) calculated by Perple_X were stacked
 281 into a three-dimensional array, $Z = (z_{1,1,1}, \dots, z_{n,w,w})$, where $w = 128$ is the resolution
 282 of the PT grid and $n = 128$ is the number of random synthetic bulk mantle composi-
 283 tions represented by a ξ value. Z was flattened into arrays of training features (PT and
 284 ξ), $X = (x_{1,1,1}, \dots, x_{v,v,v})$, and training targets (density, Vp, and Vs), $y = (y_{1,1,1}, \dots, y_{v,v,v})$,
 285 where $v = n \cdot w^2 = 128^3$ is the total number of training examples. Following common
 286 practice, X and y were scaled using “z-score normalization” before training.

287 The preprocessed training data were then fit with three different nonlinear regres-
 288 sion algorithms (Decision Tree: DT, k-Neighbors: KN, and Neural Networks: NN) from
 289 the scikit-learn python library (Pedregosa et al., 2011). Each regression algorithm was
 290 tuned with a grid search approach, where a performance score (RMSE) was evaluated
 291 over all hyperparameter combinations relevant to the particular regression algorithm (Ta-

292 ble 3). The set of hyperparameters that produced the best score (lowest RMSE) was used
 293 to train the RocMLM.

Table 3: RocMLM configuration. Hyperparameter values in parentheses are tested sequentially by a cross-validation grid search algorithm and the best set of hyperparameters is chosen by the lowest RMSE. Hyperparameters that are not shown use default values (see regression model documentation on scikit-learn.org).

Model	Hyperparameter	Value	Tuned
DT	splitter	(best, random)	tuned
	max features	(1, 2, 3)	tuned
	min samples leaf	(1, 2, 3)	tuned
	min samples split	(2, 4, 6)	tuned
KN	n neighbors	(2, 4, 8)	tuned
	weights	(uniform, distance)	tuned
NN1	hidden layer sizes	(8, 16, 32)	tuned
NN2	hidden layer sizes	([16, 16], [32, 16], [32, 32])	tuned
NN3	hidden layer sizes	([32, 16, 16], [32, 32, 16], [32, 32, 32])	tuned
NN(all)	learning rate	(0.001, 0.005, 0.001)	tuned
	batch size	20%	fixed
	max epochs	100	fixed

294 **2.4 Evaluating RocMLM Accuracy and Performance**

295 Connolly and Khan (2016) estimated the uncertainties of V_p and V_s to be on the
 296 order of 3–5% within the same thermodynamic framework used to generate RocMLM
 297 training data (Stixrude and Lithgow-Bertelloni, 2005). We can therefore consider the base-
 298 uncertainty of RocMLM predictions to be 3–5%. RocMLM predictions must also account
 299 for additional uncertainties that are introduced during RocMLM training (i.e., the vari-
 300 ance of residuals between RocMLM predictions and targets), which are about 2% for NN1
 301 and < 1% for DT, KN, and NN3. Assuming the lowest-uncertainty models (DT, KN,
 302 NN3) would be preferred for geodynamic applications, we ignore the small variances in-
 303 troduced during training (< 1%) and evaluate the total RocMLM prediction uncertain-

304 ties to be on the same order as the base GFEM uncertainty (3–5%) after Connolly and
 305 Khan (2016).

306 RocMLM accuracy (in terms of RMSE) was evaluated by: 1) testing RocMLMs
 307 on a separate validation dataset to determine the generalization capacity of RocMLMs
 308 to unseen mantle conditions (internal accuracy), and 2) comparing RocMLMs predic-
 309 tions with geophysical reference models PREM and STW105 (external accuracy). The
 310 first test evaluates the degree to which RocMLMs can reproduce GFEM predictions. The
 311 second test evaluates the degree to which the “true data” used for RocMLM training re-
 312 produces the phase transitions actually observed in Earth’s upper mantle, which depend
 313 on the thermodynamic data, GFEM algorithm, and parameterization used to describe
 314 the composition of mantle rocks (i.e., ξ).

315 The validation dataset was generated by *Perple_X* in the same manner as the train-
 316 ing dataset, but shifted by one-half step (in the positive PT directions) so that RocMLM
 317 predictions could be evaluated at completely independent PT conditions. RocMLM per-
 318 formance was evaluated by: 1) measuring single-point prediction times (execution speed),
 319 and 2) scaling execution speed by RocMLM file size (disk space) to account for infor-
 320 mation compression (model efficiency).

321 The number of PT points and synthetic bulk mantle compositions used for gener-
 322 ating training data were varied from 8 to 128 (2^{11} – 2^{21} total training examples) to test
 323 the sensitivity of RocMLM accuracy and performance with respect to the size (“capac-
 324 ity”) and composition of the training dataset. The same sets of training data were also
 325 used to evaluate single-point execution speed using a common Lookup Table approach,
 326 where a cubic spline interpolation was applied to the training dataset and rock proper-
 327 ties were evaluated at arbitrary PTX conditions. Prediction accuracy and performance
 328 were measured in a consistent manner so that direct comparisons could be made between
 329 RocMLMs, Lookup Tables, and GFEM programs.

330 **3 Results**

331 **3.1 RocMLM Accuracy**

332 The following examples of Decision Tree (DT, Figure 3), single-layer Neural Net-
 333 work (NN1, Figure 4), and three-layer Neural Network (NN3, Figure 5) models demon-

334 strate how different regression algorithms ultimately influence the accuracy of RocMLM
 335 predictions (see Supplementary Information for all regression algorithms).

336 DT predictions are practically indistinguishable from that of *Perple_X*, indicating
 337 a nearly-perfect mapping of the validation dataset by the DT algorithm (RMSE for den-
 338 sity: 0.01 g/cm³, V_p and V_s: 0.02 km/s, Figure 3). Absolute differences between *Per-*
 339 *ple_X* and DT predictions (residuals) are broadly dispersed and approach zero in most
 340 regions of PT space. Some concentrations of residuals exist near phase transitions, but
 341 are subtle and discontinuous (Figure 3g-i).

342 In contrast, NN1 predictions are notably smoother than *Perple_X* (Figure 4), with
 343 higher errors (RMSE for density: 0.02 g/cm³, V_p: 0.06 km/s, V_s: 0.05 km/s) that in-
 344 dicate an inability to resolve sharp gradients in physical properties when using a single-
 345 layer Neural Network with a small to moderate amount of neurons. This is evident by
 346 the NN1 residuals, which are systematically concentrated near phase transitions (Fig-
 347 ure 4g-i). NN1 profiles display relatively weak discontinuities with gradual changes in
 348 physical properties across the olivine → wadsleyite and ringwoodite → bridgmanite +
 349 ferropericlase transitions (Figure 4j-l), and phase transformations within the MTZ are
 350 virtually absent compared to DT and NN3 profiles. While NN1 predictions do not re-
 351 produce the validation dataset or geophysical profiles with the highest accuracy, deeper
 352 (and/or wider) NN architectures with more hidden-layers (e.g., NN3) are more capable
 353 (Figure 5). NN3 predictions fit the validation dataset and resolve discontinuities in geo-
 354 physical profiles with nearly equivalent accuracy as DT and KN algorithms (compare
 355 profiles in Supplementary Information).

356 Comparing density, V_p, and V_s depth profiles predicted by RocMLMs (for an av-
 357 erage mid-ocean ridge-like geotherm with a mantle potential temperature of 1573 K) with
 358 PREM and STW105 reveals relatively low errors (density: ≤ 0.08 g/cm³, V_p: ≤ 0.26
 359 km/s, V_s: ≤ 0.14 km/s) and high correlations ($R^2 \geq 0.94$) that indicate good agreement
 360 between seismically-derived profiles and thermodynamic predictions, irrespective of re-
 361 gression algorithm (compare profiles in the Supplementary Information). The largest de-
 362 viations between RocMLM profiles, PREM, and STW105 fall within two regions: 1) be-
 363 tween 1–8 GPa, and 2) at the base of the MTZ (Figures 3–5j-l). At pressures lower than
 364 5 GPa, the divergence between RocMLM profiles and seismically-derived profiles may
 365 be explained by the low resolution of the 1D geophysical profiles relative to the extreme

366 spatial variability in composition and geotherms on Earth. Tests using an average con-
 367 tinental geotherm to calculate RocMLM profiles results in less divergence between RocMLM
 368 profiles and PREM at < 5 GPa compared to the mid-ocean ridge-like geotherms used
 369 to build the profiles presented in Figures 3–5. At pressures between 5–8 GPa, the two
 370 geophysical models show a discrepancy: PREM contains a discontinuity, especially in
 371 seismic velocities, while STW105 has a gradual and continuous increase. RocMLM pro-
 372 files between 5–8 GPa are more similar to STW105, which does not map any disconti-
 373 nities until the olivine \rightarrow wadsleyite transition at 410 km depth (Figures 3–5j–l).

374 Within the MTZ, DT and NN3 profiles predict intermediate discontinuities, while
 375 PREM and STW105 are gradual and continuous (Figures 3,5g–i). As expected, compar-
 376 ing RocMLM profiles for different geotherms shows that the choice of a mantle poten-
 377 tial temperature leads to contrasting predictions of: 1) the overall evolution of rock prop-
 378 erties with depth, and 2) the depths, magnitudes, and sharpness of phase transitions within
 379 the MTZ (Figures 3–5g–i). RocMLM profiles show, similarly to those directly derived
 380 from the *Perple_X* calculation, temperature-sensitive discontinuities at the olivine \rightarrow wad-
 381 sleyite and wadsleyite \rightarrow ringwoodite transitions, but a rather temperature insensitive
 382 ringwoodite \rightarrow bridgmanite + ferropericlase transition (Figures 3–5g–i). This can be ex-
 383 plained by differences in Clapeyron slopes modeled by the Stixrude and Lithgow-Bertelloni
 384 (2022) dataset.

385 **3.2 RocMLM Performance**

386 We now compare RocMLM performance to two other tools classically used to pre-
 387 dict the variations of physical properties of mantle rocks in geodynamic models: GFEM
 388 programs and Lookup Tables. Note that RocMLM, GFEM, and Lookup Table perfor-
 389 mance is platform specific. Running analogous implementations with other programming
 390 languages and/or on alternative computer hardware will differ from the results presented
 391 here. All computations in this study were made using CPUs of a Macbook Pro (2022;
 392 M2 chip) with macOS 13.4 and using Python 3.11.4. All performance metrics were eval-
 393 uated with a single CPU core.

394 Figure 6 shows how execution speed, efficiency, and accuracy scale with the capac-
 395 ity of Lookup Tables and RocMLMs. Here, “capacity” refers to the number of scalar val-
 396 ues stored by Lookup Tables, or alternatively, the number of pseudosection PTX points

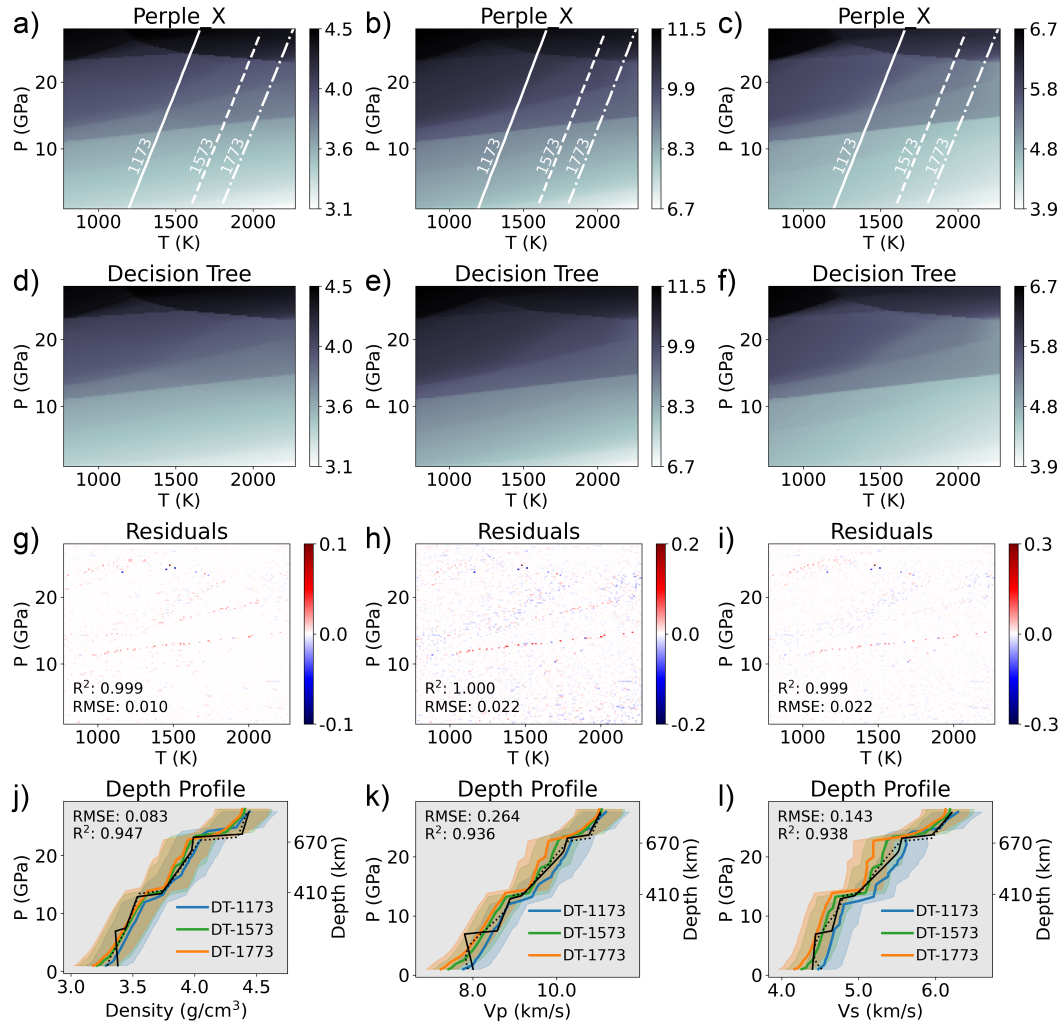


Figure 3: PT diagrams showing density (left column, g/cm³), Vp (middle column, km/s), and Vs (right column, km/s) predictions from a Perple_X model with a PUM bulk composition (a–c), a Decision Tree RocMLM (d–f), and absolute differences between Perple_X and DT (g–i) measured on the validation dataset. Depth profiles (j–l) compare Perple_X and DT predictions extracted along a 0.5 K/km adiabat with different mantle potential temperatures (white lines) with reference models PREM (solid black line, Dziewoński and Anderson, 1981) and STW105 (dotted black line, Kustowski et al., 2008). The RMSE in (j–l) indicates the measured differences between DT-1573 and PREM. Colored ribbons indicate 5% uncertainty in RocMLM predictions.

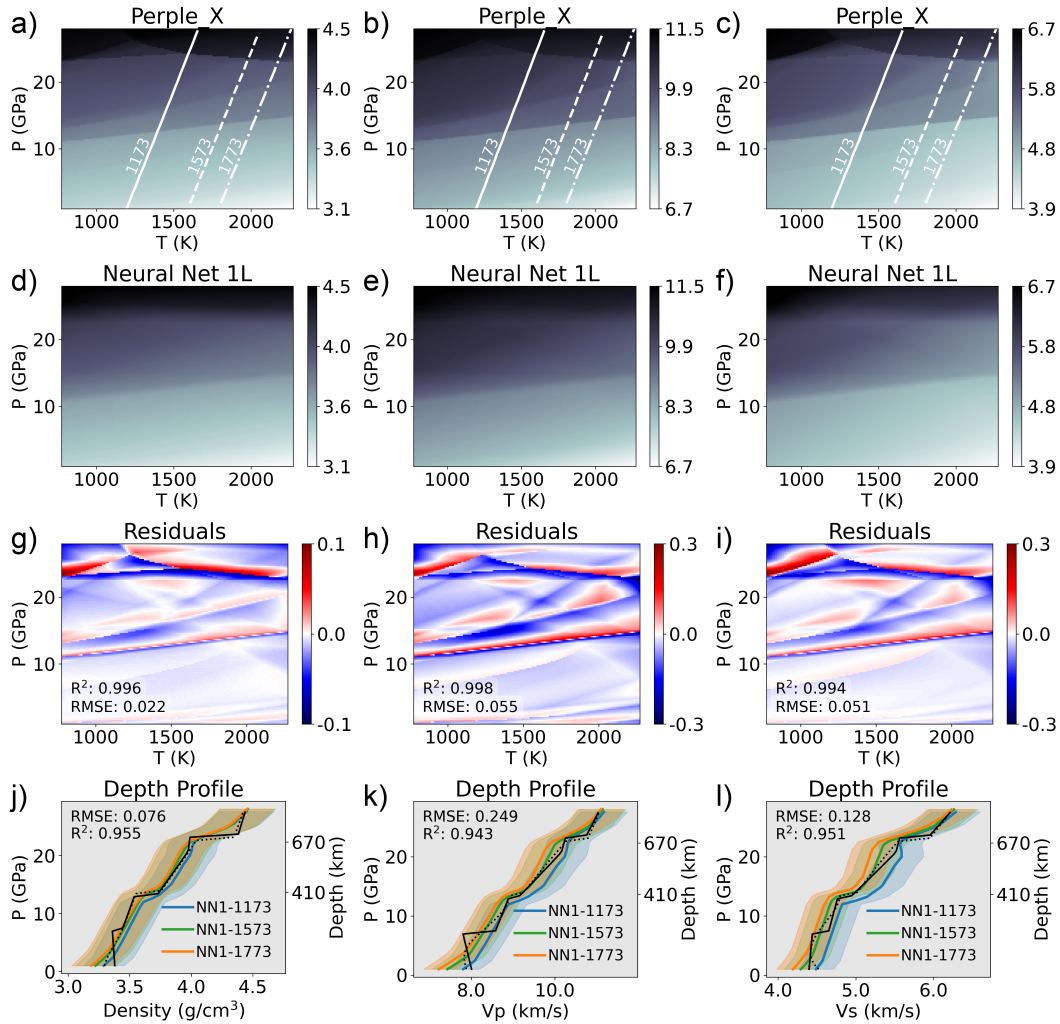


Figure 4: PT diagrams showing density (left column, g/cm^3), V_p (middle column, km/s), and V_s (right column, km/s) predictions from a Perple_X model with a PUM bulk composition (a–c), a single-layer Neural Network RocMLM (d–f), and absolute differences between Perple_X and NN1 (g–i) measured on the validation dataset. Other legend details are the same as in Figure 3.

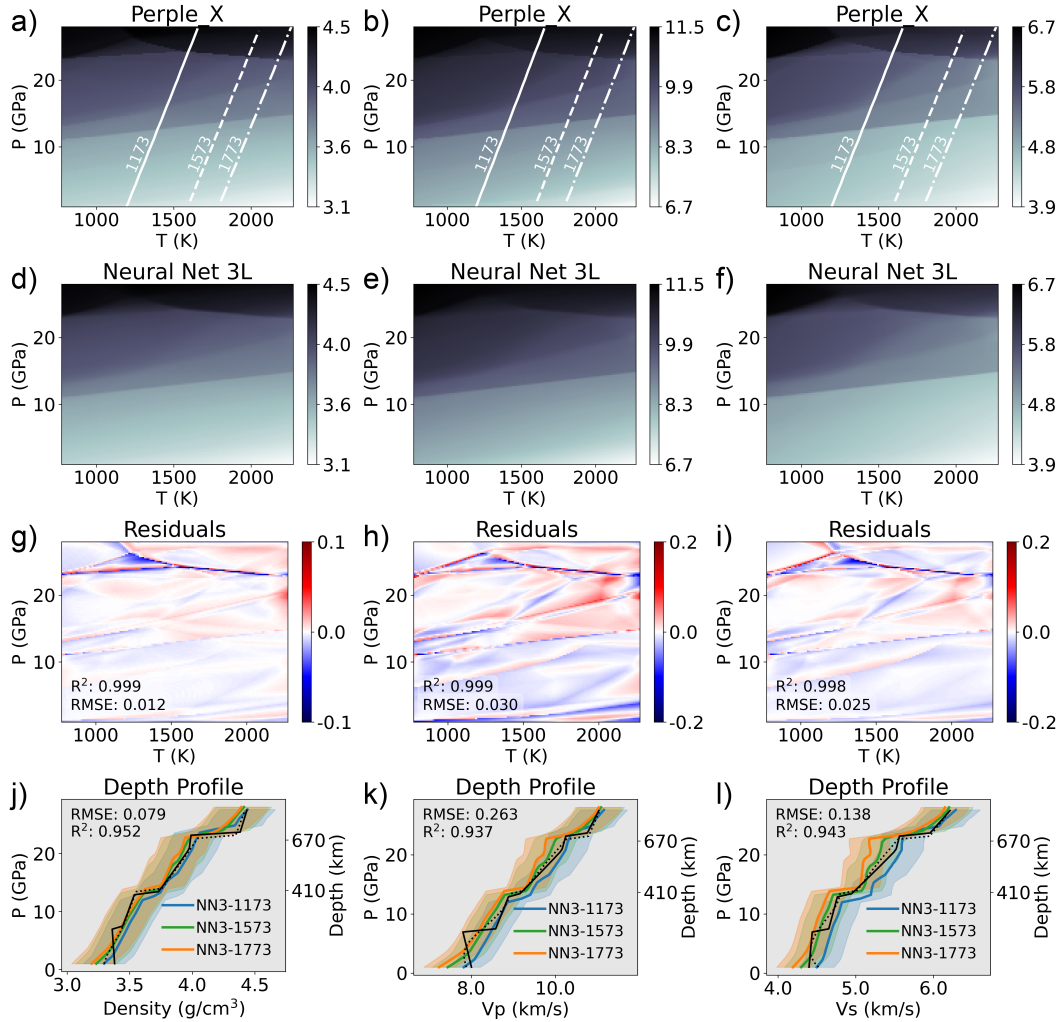


Figure 5: PT diagrams showing density (left column, g/cm^3), V_p (middle column, km/s), and V_s (right column, km/s) predictions from a *Perple_X* model with a PUM bulk composition (a–c), a three-layer Neural Network RocMLM (d–f), and absolute differences between *Perple_X* and NN3 (g–i) measured on the validation dataset. Other legend details are the same as in Figure 3.

397 “learned” by RocMLMs. Thus, “capacity” is intended to convey and compare the breadth
 398 of petrological “knowledge”, or predictive capabilities, of Lookup Tables and RocMLMs.
 399 Within the same context, the notion of “capacity” is irrelevant for GFEM programs. Rather,
 400 GFEM performance primarily scales with the number of chemical components, phase
 401 solutions, and size of the compositional space defined by the user, as well as automatic
 402 grid refinement settings and other user-defined configuration options.

403 GFEM performance is reported using the range of average execution speeds (4–228
 404 ms) and efficiencies (60–3138 ms·Mb) that we measured while generating our RocMLM
 405 training datasets as described in Section 2.2. To demonstrate the sensitivity of GFEM
 406 performance to alternative *Perple_X* configurations, we also show GFEM execution speed
 407 and efficiency for similar calculations using the thermodynamic data and phase solutions
 408 of Holland et al. (2018). Note that none of the *Perple_X* calculations using the Holland
 409 et al. (2018) configuration were used to train RocMLMs due to inaccurate seismic ve-
 410 locity predictions, and their performance metrics are only shown for illustrative purposes.

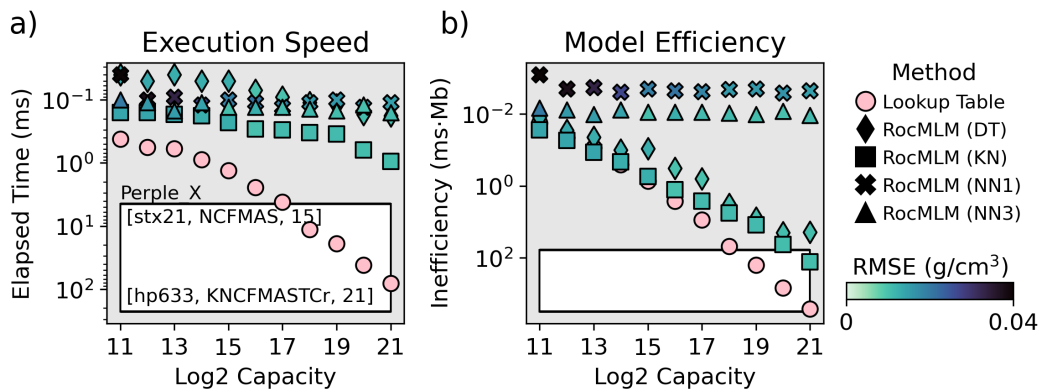


Figure 6: Computational efficiency of various approaches in terms of execution speed (a) and model efficiency (b). “Capacity” (x-axis) is a proxy for the petrological “knowledge”, or predictive capabilities, of Lookup Tables and RocMLMs. White regions indicate GFEM efficiencies for different *Perple_X* configurations (thermodynamic dataset, chemical system, and number of solution phases are indicated in square brackets). stx21: Stixrude and Lithgow-Bertelloni (2022), hp633: Holland and Powell (2011) updated in Holland et al. (2018). *Perple_X* was run without multilevel grid refinement. RMSE is measured between density predictions and the validation dataset.

411 For Lookup Tables, execution speed and efficiency both scale roughly linearly with
 412 capacity on a logarithmic scale—indicating an inverse power-law relationship between
 413 Lookup Table capacity and performance (Figure 6). RocMLM performance, in contrast,

414 scales differently depending on the performance metric and regression algorithm. For ex-
415 ample, RocMLM execution speed remains roughly constant, or increasing slightly with
416 capacity, and shows relatively small variance among all regression algorithms (0.14 ± 0.26
417 ms, 2σ , Figure 6a). Yet RocMLM efficiency is markedly different for DT and KN algo-
418 rithms compared to NN algorithms (Figure 6b). Despite the fast execution times of KN
419 and DT algorithms (Figure 6a), their efficiency scales roughly linearly with capacity on
420 a logarithmic scale—indicating an inverse power-law relationship between efficiency and
421 capacity similar to Lookup Tables (Figure 6b). NN algorithms, on the other hand, show
422 roughly constant efficiencies that indicate a high degree of information compression with-
423 out sacrificing execution speed (Figure 6b). We note that training times for NN algo-
424 rithms are many orders of magnitude larger than DT and KN algorithms (Supplemen-
425 tary Information). However, training times are neither limiting nor critical for geody-
426 namic applications as training is independent from, and precedes numerical simulations.

427 Since accuracy is measured relative to the rock properties generated by GFEM pro-
428 grams, GFEM programs have perfect accuracy by definition. With respect to RocMLMs,
429 validation accuracies (RMSE) are observed to be roughly constant for regression algo-
430 rithms that apply binary decisions or local distance-based weights (DT and KN), while
431 algorithms that apply global activation-based weights (NNs) show a positive correlation
432 between accuracy and capacity (Figure 6). In addition to improving accuracy with in-
433 creasing amounts of training examples, NN accuracy also increases with the number of
434 hidden-layers (Figure 6) because deeper networks are more capable of fitting sharp gra-
435 dients in the training data (see Supplementary Information for examples of NN1, NN2,
436 and NN3 RocMLMs). We also tested the effects of NN width (changing the number of
437 nodes within each hidden layer), but this had a negligible impact on NN performance
438 and accuracy compared to increasing NN depth.

439 **4 Discussion**

440 **4.1 RocMLM Performance Tradeoffs**

441 RocMLM performance and accuracy are both critical for geodynamic applications
442 and crucial for determining if RocMLMs are an improvement over methods commonly
443 used for predicting rock properties in numerical geodynamic simulations. In terms of pure
444 execution speed, our testing demonstrates that RocMLMs can make predictions between

445 10^1 – 10^3 times faster than GFEM programs and Lookup Tables (Figure 6), depending
446 on the GFEM program configuration. The difference in execution speed between Lookup
447 Tables and RocMLMs is small for low-resolution models (Figure 6) that are limited to
448 ≤ 16 mantle compositions and large PT intervals (≥ 1.7 GPa and 100 K PT step sizes).
449 However, such low-resolution models are not an obvious improvement over simple poly-
450 nomial approximations of a selective number of important phase transformations. At higher
451 resolutions, RocMLMs can accurately resolve the physical properties of all thermodynamically-
452 stable mineral assemblages in fine detail (at PT intervals of ≤ 0.2 GPa and 12 K) and
453 for a wide variety of bulk mantle compositions (Figure 2). In addition to their broad pre-
454 dictive capabilities, high-resolution RocMLMs make predictions at speeds (approximately
455 0.1–1 ms, Figure 6) that allow computation of physical properties at the node-scale dur-
456 ing geodynamic simulations. We therefore argue that high-resolution RocMLMs over-
457 come all practical limitations for implementing thermodynamically self-consistent den-
458 sity evolution in numerical geodynamic models.

459 With respect to ranking the practicality of different RocMLM for geodynamic ap-
460 plications, execution speeds and accuracies alone suggest that high-resolution RocMLMs
461 will perform with roughly equivalent outcomes regardless of the regression algorithm (Fig-
462 ure 6a). However, our testing reveals an obvious tradeoff between RocMLM performance
463 and accuracy when accounting for compression ratio (i.e., the amount of “learned” in-
464 formation relative to the RocMLM file size). Figure 6b shows DT and KN algorithms
465 becoming rapidly inefficient compared to NNs as the capacity of the training dataset in-
466 creases. This is because NN algorithms require relatively little information to make pre-
467 dictions after training (weights and biases for each neuron) compared to DT (tree struc-
468 ture: nodes, splits, and predictions) and KN (entire training dataset with distance weights)
469 algorithms. Moreover, accuracy tends to improve monotonically with dataset capacity
470 for NN, but not for DT or KN. We therefore argue that deep NN RocMLMs are the most
471 practical choice for geodynamic applications for three reasons: 1) modeling more rock
472 types only requires adding more training data, 2) adding more training data improves
473 prediction accuracy without diminishing performance, and 3) further improvements and
474 adaptations to different geodynamic applications are possible by exploring different ar-
475 chitectures than the simple NN models we have tested thus far.

476 The main limitations of NN RocMLMs are twofold: 1) training is computationally
477 expensive compared to other regression algorithms (Supplementary Information) and 2)

478 shallow NN architectures imply smoother gradients in rock properties than GFEM cal-
 479 culations. We do not consider these limitations critical because training time is indepen-
 480 dent from RocMLM performance and even if deeper NN architectures are needed to fit
 481 discontinuities in rock properties with high accuracy, the number of layers and neurons
 482 in each layer remains small (Table 3). We note that our testing has been limited to the
 483 prediction of three properties that are mostly P-dependent and are relatively continu-
 484 ous despite a few large discontinuities. In principle, RocMLMs can be trained on any ther-
 485 modynamic variable output by GFEM programs. However, we have not yet trained RocMLMs
 486 on more discrete, discontinuous, and/or highly T-dependent variables, such as modal pro-
 487 portions of minerals, volatile contents, or melt fraction, which will be treated in future
 488 developments of RocMLMs.

489 4.2 Geophysical and Thermodynamic Estimates of Elastic Properties

490 The amount of overlap between RocMLM profiles and PREM (Figures 3–3) sug-
 491 gests good agreement between thermodynamic and geophysical estimates of the elastic
 492 properties of mantle rocks within the limits of our training dataset and *Perple_X* con-
 493 figuration (see Sections 2.1 and 2.2). Discrepancies between thermodynamic profiles and
 494 PREM can be explained by chemical heterogeneity and/or differences in mantle geotherms
 495 that modify phase relations (Goes et al., 2022; Karki and Stixrude, 1999; Karki et al.,
 496 2001; Stixrude and Lithgow-Bertelloni, 2012; Waszek et al., 2021; Xu et al., 2008). Be-
 497 cause the RocMLM training dataset spans a wide array of synthetic bulk mantle com-
 498 positions, we can directly test the sensitivity of thermodynamic estimates to changes in
 499 bulk FeO–MgO contents (Figure 7).

500 As Fertility Index (ξ) increases by refertilization and/or lack of melt extraction and
 501 the bulk mantle composition becomes more Fe-rich (and more dense), V_p and V_s respond
 502 (both positively and negatively) according to the equations of state described in Stixrude
 503 and Lithgow-Bertelloni (2005). RocMLM training data show that density is the least sen-
 504 sitive parameter to ξ overall with only modest variations across a broad range of man-
 505 tle rocks from fertile to highly depleted ($\xi = 0.76$, Figure 7a). The largest density vari-
 506 ations occur at pressures below the olivine \rightarrow wadsleyite transition (< 410 km), yet are
 507 still small enough (approximately 3–5 %) to imply that spontaneous mantle convection
 508 requires strong thermal gradients and/or hydration by metamorphic fluids in addition
 509 to melt extraction.

510 In contrast to density, V_p and V_s are more sensitive to ξ overall, especially at pressures
 511 above the olivine \rightarrow wadsleyite transition (> 410 km). RocMLM training data sug-
 512 gests that an “optimal” V_p/V_s profile requires a more depleted mantle between 410–670
 513 km and a more fertile mantle at < 410 km (Figure 7b,c). Forming this compositional
 514 layering pattern is counterintuitive, however, as partial melting is expected to be more
 515 pervasive at lower pressures. Moreover, density profiles are incongruent with this pat-
 516 tern, suggesting instead that a depleted mantle at < 410 km and more fertile mantle at
 517 > 410 km are required for an optimal fit with PREM and STW105 (Figure 7a).

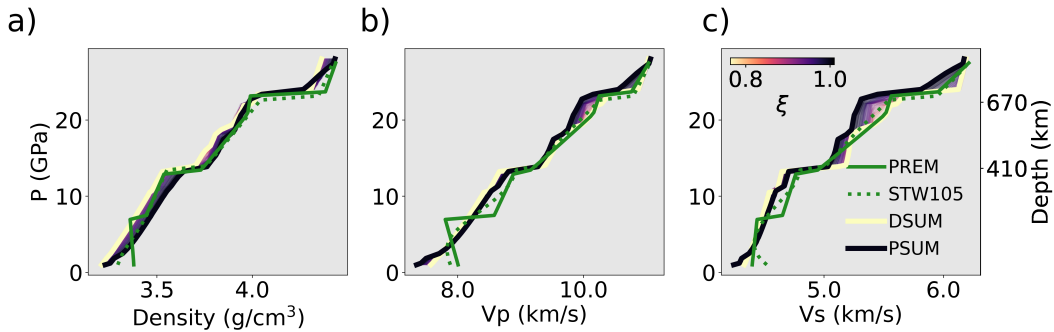


Figure 7: Depth profiles of RocMLM training data along a 1573 K mantle adiabat showing the sensitivities of thermodynamic estimates of density (a), V_p (b), and V_s (c) to changes in bulk mantle composition (as represented by the Fertility Index, ξ). Geophysical profiles PREM and STW105 (green lines) and the profiles of synthetic mantle end-member compositions PSUM and DSUM (thick colored lines) are shown for reference. Thin colored lines show profiles for the entire range of RocMLM training data.

518 5 Conclusions

519 The dynamics of Earth’s upper mantle is largely driven by density contrasts stem-
 520 ming from changes in PT conditions, which lead to phase transformations in mantle rocks.
 521 These phase transformations also modify the elastic properties of mantle rocks. There-
 522 fore phase changes must be considered when inverting present-day mantle structure from
 523 seismic data. Likewise, numerical geodynamic simulations of mantle convection must ac-
 524 count for thermodynamics, but are typically implemented with simple PT-dependent pa-
 525 rameterizations of rock properties and phase boundaries that do not explicitly account
 526 for changes in Gibbs Free Energy resulting from changes in PT and in bulk composition.
 527 Here, we introduce RocMLMs as an alternative to GFEM programs and we evaluate RocMLM
 528 performance and accuracy. We also show how the RocMLM predictions compare to PREM
 529 and STW105. Our main findings are as follows:

- 530 1. RocMLMs predict density and elastic properties with high accuracy and are up
531 to 101–103 faster than commonly used methods. This improvement in prediction
532 speed makes thermodynamically self-consistent mantle convection within high-resolution
533 numerical geodynamic models practical for the first time.
- 534 2. RocMLMs trained with moderately deep (3 hidden layers) NNs are more robust
535 and efficient compared to RocMLMs trained with other regression algorithms, and
536 are therefore the most practical models for coupling with numerical geodynamic
537 codes.
- 538 3. RocMLM training data are sensitive to bulk mantle composition and geothermal
539 gradients, yet show good agreement with PREM and STW105 for an average man-
540 tle geotherm.

541 Based on our results, we argue that moderately deep NN RocMLMs can be excep-
542 tional emulators of GFEM programs in geodynamic simulations that require computa-
543 tionally efficient predictions of rock properties. We have demonstrated that RocMLMs
544 perform remarkably well for dry mantle rocks with compositions ranging from very fer-
545 tile lherzolites to strongly depleted harzburgites and PT conditions ranging from 1–28
546 GPa and 773–2273 K.

547 Moreover, the RocMLM approach can be used with any GFEM program and ther-
548 modynamic dataset. Any improvement to the underlying thermodynamic data should
549 further increase the accuracy of RocMLM predictions. Testing RocMLMs predictions
550 on other thermodynamic variables of interest, including modal proportions of minerals,
551 volatile contents, and melt fractions will be the focus of future studies. Likewise, in fu-
552 ture works, we will extend the training data to include hydrous systems and additional
553 end-member mantle compositions (e.g., pyroxenites and dunites).

554 **6 Acknowledgements**

555 This work was supported by the Tremplin-ERC grant LEARNING awarded to Nestor
556 Cerpa by the I-SITE excellence program at the Université de Montpellier. We thank Mau-
557 rine Montagnat, Fernando Carazo, Nicolas Berlie, and many researchers and students
558 at Géosciences Montpellier for their thoughtful feedback during the development of this
559 work. We gratefully acknowledge additional support from the European Research Coun-

560 cil (ERC) under the European Union Horizon 2020 Research and Innovation program
561 grant agreement No. 882450 (ERC RhEoVOLUTION) awarded to Andréa Tommasi.

562 **7 Open Research**

563 All data, code, and relevant information for reproducing this work can be found
564 at https://github.com/buchanankerswell/kerswell_et_al_rocmlm, and at <https://doi.org/10.17605/OSF.IO/K23TB>, the official Open Science Framework data repository
565 (Kerswell et al., 2024). All code is MIT Licensed and free for use and distribution (see
566 license details). Reference models PREM and STW105 are freely available from the In-
567 corporated Research Institutions for Seismology Earth Model Collaboration (IRIS EMC,
568 doi: 10.17611/DP/EMC.1, Trabant et al., 2012). All computations were made using CPUs
569 of a Macbook Pro (2022; M2 chip) with macOS 13.4 and using Python 3.11.4.
570

571 **8 References**

References

- 572
- 573 Agrusta, R., Goes, S., and van Hunen, J. (2017). Subducting-slab transition-zone
574 interaction: Stagnation, penetration and mode switches. *Earth and Planetary
575 Science Letters*, 464:10–23.
- 576 Agrusta, R., Tommasi, A., Arcay, D., Gonzalez, A., and Gerya, T. (2015). How
577 partial melting affects small-scale convection in a plume-fed sublithospheric
578 layer beneath fast-moving plates. *Geochemistry, Geophysics, Geosystems*,
579 16(11):3924–3945.
- 580 Akaogi, M., Ito, E., and Navrotsky, A. (1989). Olivine-modified spinel-spinel transi-
581 tions in the system $\text{mg}_2\text{SiO}_4\text{-Fe}_2\text{SiO}_4$: Calorimetric measurements, thermochem-
582 ical calculation, and geophysical application. *Journal of Geophysical Research: Solid Earth*,
583 94(B11):15671–15685.
- 584 Akaogi, M., Takayama, H., Kojitani, H., Kawaji, H., and Atake, T. (2007). Low-
585 temperature heat capacities, entropies and enthalpies of mg_2SiO_4 poly-
586 morphs, and α - β - γ and post-spinel phase relations at high pressure. *Physics
587 and Chemistry of Minerals*, 34:169–183.
- 588 Ballmer, M., Schmerr, N., Nakagawa, T., and Ritsema, J. (2015). Compositional
589 mantle layering revealed by slab stagnation at ~ 1000 -km depth. *Science ad-
590 vances*, 1(11):e1500815.
- 591 Bina, C. and Helffrich, G. (1994). Phase transition clapeyron slopes and transition
592 zone seismic discontinuity topography. *Journal of Geophysical Research: Solid
593 Earth*, 99(B8):15853–15860.
- 594 Brown, E. and Leshner, C. (2016). Reebop: a forward model simulating melting
595 of thermally and lithologically variable upwelling mantle. *Geochemistry, Geo-
596 physics, Geosystems*, 17(10):3929–3968.
- 597 Cagnioncle, A., Parmentier, E., and Elkins-Tanton, L. (2007). Effect of solid flow
598 above a subducting slab on water distribution and melting at convergent plate
599 boundaries. *Journal of Geophysical Research: Solid Earth*, 112(B9).
- 600 Cerpa, N., Arcay, D., and Padrón-Navarta, J. (2022). Sea-level stability over geolog-
601 ical time owing to limited deep subduction of hydrated mantle. *Nature Geo-
602 science*, 15(5):423–428.
- 603 Cerpa, N., Wada, I., and Wilson, C. (2019). Effects of fluid influx, fluid viscosity,
604 and fluid density on fluid migration in the mantle wedge and their implications

- 605 for hydrous melting. *Geosphere*, 15(1):1–23.
- 606 Christensen, U. (1995). Effects of phase transitions on mantle convection. *Annual*
607 *Review of Earth and Planetary Sciences*, 23(1):65–87.
- 608 Čížková, H. and Bina, C. (2013). Effects of mantle and subduction-interface rheolo-
609 gies on slab stagnation and trench rollback. *Earth and Planetary Science Let-*
610 *ters*, 379:95–103.
- 611 Connolly, J. (2009). The geodynamic equation of state: what and how. *Geochem-*
612 *istry, geophysics, geosystems*, 10(10).
- 613 Connolly, J. and Kerrick, D. (2002). Metamorphic controls on seismic velocity of
614 subducted oceanic crust at 100–250 km depth. *Earth and Planetary Science*
615 *Letters*, 204(1-2):61–74.
- 616 Connolly, J. and Khan, A. (2016). Uncertainty of mantle geophysical properties
617 computed from phase equilibrium models. *Geophysical Research Letters*,
618 43(10):5026–5034.
- 619 Dziewoński, A. and Anderson, D. (1981). Preliminary reference earth model. *Physics*
620 *of the earth and planetary interiors*, 25(4):297–356.
- 621 Fukao, Y., Widiyantoro, S., and Obayashi, M. (2001). Stagnant slabs in the upper
622 and lower mantle transition region. *Reviews of Geophysics*, 39(3):291–323.
- 623 Gerya, T. and Meilick, F. (2011). Geodynamic regimes of subduction under an ac-
624 tive margin: effects of rheological weakening by fluids and melts. *Journal of*
625 *Metamorphic Geology*, 29(1):7–31.
- 626 Gerya, T. and Yuen, D. (2003). Rayleigh–Taylor instabilities from hydration and
627 melting propel ‘cold plumes’ at subduction zones. *Earth and Planetary Science*
628 *Letters*, 212(1-2):47–62.
- 629 Gibbs, J. (1878). On the equilibrium of heterogeneous substances. *American Journal*
630 *of Science*, 3(96):441–458.
- 631 Goes, S., Yu, C., Ballmer, M., Yan, J., and van der Hilst, R. (2022). Compositional
632 heterogeneity in the mantle transition zone. *Nature Reviews Earth & Environ-*
633 *ment*, 3(8):533–550.
- 634 Green, D. (1979). Petrogenesis of mid ocean ridge basalts. *The Earth: its origin,*
635 *structure and evolution*, pages 200–299.
- 636 Hirose, K. (2002). Phase transitions in pyrolitic mantle around 670-km depth: Impli-
637 cations for upwelling of plumes from the lower mantle. *Journal of Geophysical*

- 638 *Research: Solid Earth*, 107(B4):ECV–3.
- 639 Holland, T., Green, E., and Powell, R. (2018). Melting of peridotites through to
640 granites: a simple thermodynamic model in the system kncfmashtocr. *Journal*
641 *of Petrology*, 59(5):881–900.
- 642 Holland, T. and Powell, R. (2001). Calculation of phase relations involving haplo-
643 granitic melts using an internally consistent thermodynamic dataset. *Journal*
644 *of Petrology*, 42(4):673–683.
- 645 Holland, T. and Powell, R. (2011). An improved and extended internally consistent
646 thermodynamic dataset for phases of petrological interest, involving a new
647 equation of state for solids. *Journal of metamorphic Geology*, 29(3):333–383.
- 648 Ishii, T., Huang, R., Fei, H., Koemets, I., Liu, Z., Maeda, F., Yuan, L., Wang, L.,
649 Druzhbin, D., Yamamoto, T., et al. (2018). Complete agreement of the post-
650 spinel transition with the 660-km seismic discontinuity. *Scientific reports*,
651 8(1):6358.
- 652 Ita, J. and Stixrude, L. (1992). Petrology, elasticity, and composition of the mantle
653 transition zone. *Journal of Geophysical Research: Solid Earth*, 97(B5):6849–
654 6866.
- 655 Ito, E. (1982). Stability relations of silicate spinels, ilmenites, and perovskite. *High*
656 *pressure research in geophysics*, pages 405–419.
- 657 Ito, E., Akaogi, M., Topor, L., and Navrotsky, A. (1990). Negative pressure-
658 temperature slopes for reactions forming mgsio₃ perovskite from calorimetry.
659 *Science*, 249(4974):1275–1278.
- 660 Ito, E. and Katsura, T. (1989). A temperature profile of the mantle transition zone.
661 *Geophysical Research Letters*, 16(5):425–428.
- 662 Ito, E. and Takahashi, E. (1989). Postspinel transformations in the system mg₂siO₄-
663 fe₂siO₄ and some geophysical implications. *Journal of Geophysical Research:*
664 *Solid Earth*, 94(B8):10637–10646.
- 665 Jenkins, J., Cottaar, S., White, R., and Deuss, A. (2016). Depressed mantle disconti-
666 nities beneath iceland: Evidence of a garnet controlled 660 km discontinuity?
667 *Earth and Planetary Science Letters*, 433:159–168.
- 668 Karato, S., Riedel, M., and Yuen, D. (2001). Rheological structure and deformation
669 of subducted slabs in the mantle transition zone: implications for mantle cir-
670 culation and deep earthquakes. *Physics of the Earth and Planetary Interiors*,

- 671 127(1-4):83–108.
- 672 Karki, B. and Stixrude, L. (1999). Seismic velocities of major silicate and oxide
673 phases of the lower mantle. *Journal of Geophysical Research: Solid Earth*,
674 104(B6):13025–13033.
- 675 Karki, B., Stixrude, L., and Wentzcovitch, R. (2001). High-pressure elastic proper-
676 ties of major materials of earth’s mantle from first principles. *Reviews of Geo-*
677 *physics*, 39(4):507–534.
- 678 Katsura, T. and Ito, E. (1989). The system $\text{mg}_2\text{SiO}_4\text{-Fe}_2\text{SiO}_4$ at high pressures and
679 temperatures: Precise determination of stabilities of olivine, modified spinel,
680 and spinel. *Journal of Geophysical Research: Solid Earth*, 94(B11):15663–
681 15670.
- 682 Katsura, T., Yamada, H., Shinmei, T., Kubo, A., Ono, S., Kanzaki, M., Yoneda,
683 A., Walter, M., Ito, E., Urakawa, S., et al. (2003). Post-spinel transition in
684 mg_2SiO_4 determined by high p–t in situ x-ray diffractometry. *Physics of the*
685 *Earth and Planetary Interiors*, 136(1-2):11–24.
- 686 Kelley, K., Plank, T., Newman, S., Stolper, E., Grove, T., Parman, S., and Hauri,
687 E. (2010). Mantle melting as a function of water content beneath the mariana
688 arc. *Journal of Petrology*, 51(8):1711–1738.
- 689 Kerswell, B., Cerpa, N., Tommasi, A., Godard, M., and Padrón-Navarta, J. (2024).
690 RocMLMs: Predicting rock properties through machine learning models
691 [dataset repository].
- 692 Kerswell, B., Kohn, M., and Gerya, T. (2021). Backarc lithospheric thickness and
693 serpentine stability control slab-mantle coupling depths in subduction zones.
694 *Geochemistry, Geophysics, Geosystems*, 22(6):e2020GC009304.
- 695 Kuritani, T., Xia, Q., Kimura, J., Liu, J., Shimizu, K., Ushikubo, T., Zhao, D., Nak-
696 agawa, M., and Yoshimura, S. (2019). Buoyant hydrous mantle plume from the
697 mantle transition zone. *Scientific Reports*, 9(1):6549.
- 698 Kustowski, B., Ekström, G., and Dziewoński, A. (2008). Anisotropic shear-wave ve-
699 locity structure of the earth’s mantle: A global model. *Journal of Geophysical*
700 *Research: Solid Earth*, 113(B6).
- 701 Le Roux, V., Bodinier, J., Tommasi, A., Alard, O., Dautria, J., Vauchez, A., and
702 Riches, A. (2007). The lherz spinel lherzolite: refertilized rather than pristine
703 mantle. *Earth and Planetary Science Letters*, 259(3-4):599–612.

- 704 Li, Z., Gerya, T., and Connolly, J. (2019). Variability of subducting slab morpholo-
 705 gies in the mantle transition zone: Insight from petrological-thermomechanical
 706 modeling. *Earth-Science Reviews*, 196:102874.
- 707 Litasov, K., Ohtani, E., Sano, A., Suzuki, A., and Funakoshi, K. (2005). Wet sub-
 708 duction versus cold subduction. *Geophysical Research Letters*, 32(13).
- 709 Liu, M., Yuen, D., Zhao, W., and Honda, S. (1991). Development of diapiric struc-
 710 tures in the upper mantle due to phase transitions. *Science*, 252(5014):1836–
 711 1839.
- 712 Maruyama, S., Liou, J., and Terabayashi, M. (1996). Blueschists and eclogites of the
 713 world and their exhumation. *International geology review*, 38(6):485–594.
- 714 Morishima, H., Kato, T., Suto, M., Ohtani, E., Urakawa, S., Utsumi, W., Shimo-
 715 mura, O., and Kikegawa, T. (1994). The phase boundary between α - and
 716 β -Mg₂SiO₄ determined by in situ x-ray observation. *Science*, 265(5176):1202–
 717 1203.
- 718 Nakagawa, T. and Buffett, B. (2005). Mass transport mechanism between the upper
 719 and lower mantle in numerical simulations of thermochemical mantle convec-
 720 tion with multicomponent phase changes. *Earth and Planetary Science Letters*,
 721 230(1-2):11–27.
- 722 Pedregosa, F., Varoquaux, G., Gramfort, A., Michel, V., Thirion, B., Grisel, O.,
 723 Blondel, M., Prettenhofer, P., Weiss, R., Dubourg, V., Vanderplas, J., Pas-
 724 sos, A., Cournapeau, D., Brucher, M., Perrot, M., and Duchesnay, E. (2011).
 725 Scikit-learn: Machine learning in Python. *Journal of Machine Learning Re-*
 726 *search*, 12:2825–2830.
- 727 Riel, N., Kaus, B., Green, E., and Berlie, N. (2022). Magemin, an efficient gibbs
 728 energy minimizer: application to igneous systems. *Geochemistry, Geophysics,*
 729 *Geosystems*, 23(7):e2022GC010427.
- 730 Ringwood, A. (1991). Phase transformations and their bearing on the constitution
 731 and dynamics of the mantle. *Geochimica et Cosmochimica Acta*, 55(8):2083–
 732 2110.
- 733 Schubert, G., Yuen, D., and Turcotte, D. (1975). Role of phase transitions in a dy-
 734 namic mantle. *Geophysical Journal International*, 42(2):705–735.
- 735 Shaw, D. (1970). Trace element fractionation during anatexis. *Geochimica et Cos-*
 736 *mochimica Acta*, 34(2):237–243.

- 737 Sizova, E., Gerya, T., Brown, M., and Perchuk, L. (2010). Subduction styles in the
738 precambrian: insight from numerical experiments. *Lithos*, 116(3-4):209–229.
- 739 Spear, F. (1993). Metamorphic phase equilibria and pressure-temperature-time
740 paths. *Mineralogical Society of America Monograph*, 799.
- 741 Stixrude, L. and Lithgow-Bertelloni, C. (2005). Thermodynamics of mantle miner-
742 als—i. physical properties. *Geophysical Journal International*, 162(2):610–632.
- 743 Stixrude, L. and Lithgow-Bertelloni, C. (2012). Geophysics of chemical heterogeneity
744 in the mantle. *Annual Review of Earth and Planetary Sciences*, 40:569–595.
- 745 Stixrude, L. and Lithgow-Bertelloni, C. (2022). Thermal expansivity, heat ca-
746 pacity and bulk modulus of the mantle. *Geophysical Journal International*,
747 228(2):1119–1149.
- 748 Sun, S. and McDonough, W. (1989). Chemical and isotopic systematics of oceanic
749 basalts: implications for mantle composition and processes. *Geological Society,*
750 *London, Special Publications*, 42(1):313–345.
- 751 Syracuse, E., van Keken, P., and Abers, G. (2010). The global range of subduction
752 zone thermal models. *Physics of the Earth and Planetary Interiors*, 183(1-
753 2):73–90.
- 754 Tackley, P., Stevenson, D., Glatzmaier, G., and Schubert, G. (1994). Effects of mul-
755 tiple phase transitions in a three-dimensional spherical model of convection in
756 earth’s mantle. *Journal of Geophysical Research: Solid Earth*, 99(B8):15877–
757 15901.
- 758 Tackley, P. and Xie, S. (2003). Stag3d: a code for modeling thermo-chemical multi-
759 phase convection in earth’s mantle. In *Computational Fluid and Solid Mechan-*
760 *ics 2003*, pages 1524–1527. Elsevier.
- 761 Torii, Y. and Yoshioka, S. (2007). Physical conditions producing slab stagnation:
762 Constraints of the clapeyron slope, mantle viscosity, trench retreat, and dip
763 angles. *Tectonophysics*, 445(3-4):200–209.
- 764 Trabant, C., Hutko, A., Bahavar, M., Karstens, R., Ahern, T., and Aster, R. (2012).
765 Data products at the iris dmc: Stepping stones for research and other applica-
766 tions. *Seismological Research Letters*, 83(5):846–854.
- 767 Wang, X., Wilde, S., Li, Q., and Yang, Y. (2015). Continental flood basalts derived
768 from the hydrous mantle transition zone. *Nature Communications*, 6(1):7700.

- 769 Waszek, L., Tauzin, B., Schmerr, N., Ballmer, M., and Afonso, J. (2021). A poorly
770 mixed mantle transition zone and its thermal state inferred from seismic
771 waves. *Nature Geoscience*, 14(12):949–955.
- 772 Workman, R. and Hart, S. (2005). Major and trace element composition of the de-
773pleted morb mantle (dmm). *Earth and Planetary Science Letters*, 231(1-2):53–
774 72.
- 775 Xu, W., Lithgow-Bertelloni, C., Stixrude, L., and Ritsema, J. (2008). The effect of
776 bulk composition and temperature on mantle seismic structure. *Earth and*
777 *Planetary Science Letters*, 275(1-2):70–79.
- 778 Yang, J. and Faccenda, M. (2020). Intraplate volcanism originating from upwelling
779 hydrous mantle transition zone. *Nature*, 579(7797):88–91.